Nanoscale strain-induced pair suppression as a vortex-pinning mechanism in high-temperature superconductors

A. Llordés[1], A. Palau[1], J. Gázquez[1,2], M. Coll[1], R. Vlad[1], A. Pomar[1], J. Arbiol[1,3], R. Guzmán[1], S. Ye[1], V. Rouco[1], F. Sandiumenge[1], S. Ricart[1], T. Puig[1], M. Varela[2], D. Chateigner[4], J. Vanacken[5], J. Gutiérrez[5], V. Moshchalkov[5], G. Deutscher[6], C. Magen[7] and X. Obradors[1]*

Boosting large-scale superconductor applications require nanostructured conductors with artificial pinning centres immobilizing quantized vortices at high temperature and magnetic fields. Here we demonstrate a highly effective mechanism of artificial pinning centres in solution-derived high-temperature superconductor nanocomposites through generation of nanostrained regions where Cooper pair formation is suppressed. The nanostrained regions identified from transmission electron microscopy devise a very high concentration of partial dislocations associated with intergrowths generated between the randomly oriented nanodots and the epitaxial $YBa_2Cu_3O_7$ matrix. Consequently, an outstanding vortex-pinning enhancement correlated to the nanostrain is demonstrated for four types of randomly oriented nanodot, and a unique evolution towards an isotropic vortex-pinning behaviour, even in the effective anisotropy, is achieved as the nanostrain turns isotropic. We suggest a new vortex-pinning mechanism based on the bond-contraction pairing model, where pair formation is quenched under tensile strain, forming new and effective core-pinning regions.

The search for effective methodologies of pinning vortices in superconductors has been one of the most important topics since the discovery of type II superconductors, more than 50 years ago. This is because the most highly appreciated property of superconductors, that is, dissipationless current flow, is truncated in the mixed state of type II superconductors unless vortices are pinned[1]. Localization of the vortices' core at non-superconducting regions of dimensions of the order of ξ, the coherence length, is the most efficient vortex-pinning mechanism. For this reason a large variety of nanocomposite high-temperature superconductor (HTS) materials have been recently prepared with the purpose of using the normal-state volume of a second non-superconducting phase as localization centres for vortices, that is, artificial pinning centres. This mechanism has indeed turned out to be effective, but in other cases defects induced within the $YBa_2Cu_3O_7$ (YBCO) matrix due to these inclusions have been proposed to play the relevant role[2].

Seminal works have shown that phase-separated YBCO nano composites[2,3] opened up a completely new arena for nanoengineering HTS thin films and coated conductors demonstrating enhanced vortex pinning[4–9]. Vortex matter in HTS materials has a complex behaviour[10]; for this reason, it becomes a tantalizing task to specifically engineer the secondary phases.

Nanocomposite HTS materials have opened a new path towards the realization of enhanced vortex pinning in HTSs. However, up to now, the strategy has been always to generate controlled nanosized spared volumes of non-superconducting secondary crystalline phases. *In situ*-grown nanocomposite films are suitable to use epitaxial nanodots and hence very detailed knowledge about self-organization principles is required to prepare optimized materials[4,5,11–13]. In *ex situ*-grown nanocomposites, instead, the nanodots are mostly randomly oriented, whereas the YBCO matrix remains epitaxial, thus generating incoherent interfaces[2,14]. The consequences of this very uncommon structure to the YBCO lattice extend to a much longer range than in epitaxial nanocomposites and it generates inhomogeneous strain (nanostrain). The influence of strain on vortex pinning in HTSs has been noticed experimentally recently[15,16]; however, the exact role of incoherent interfaces as a source for enhanced vortex pinning of the YBCO lattice and its correlation with strain has not been clarified up to now, in spite of its extreme effectiveness[2].

In the present work we explore a wide range of YBCO nanocomposite compositions, prepared by chemical solution deposition (CSD), and we demonstrate that nanostrain is proportional to the incoherent specific interface (interface per unit volume) of the nanodots. A strong enhancement of vortex pinning is found to be controlled by nanostrain, which becomes isotropic and induces a vanishing effective anisotropy of the isotropic contribution to the critical currents. A new vortex-pinning mechanism based on strain-induced Cooper pair suppression is proposed[17,18], predicting that a quasi-isotropic vortex pinning landscape is generated within the YBCO matrix itself. This isotropic pinning contribution is achieved in spite of the fact that the intrinsic mass anisotropy of

[1]Institut de Ciència de Materials de Barcelona, ICMAB-CSIC, Campus de la UAB, 08193 Bellaterra, Catalonia, Spain, [2]Materials Science & Technology Division, Oak Ridge National Laboratory, Oak Ridge, Tennessee 37831, USA, [3]Institució Catalana de Recerca i Estudis Avançats (ICREA), 08010 Barcelona, Catalonia, Spain, [4]Laboratoire de Cristallographie et Sciences des Matériaux, CRISMAT, ENSICAEN, IUT-Caen, Université de Caen Basse-Normandie, 6 boulevard Maréchal Juin, 14050 Caen Cedex 4, France, [5]INPAC-Institute for Nanoscale Physics and Chemistry, Pulsed Field Group, K.U. Leuven, Celestijnenlaan 200 D, B-3001 Leuven, Belgium, [6]School of Physics and Astronomy, Tel Aviv University, Tel Aviv 69978, Israel, [7]Universidad de Zaragoza, Instituto de Nanociencia de Aragon, Zaragoza 50018, Spain. *e-mail: Xavier.obradors@icmab.es.
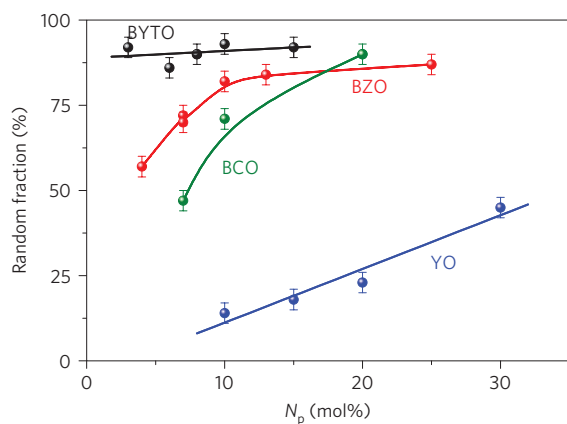
Figure 1 | XRD analysis to quantify the random and epitaxial fraction of nanodots in the nanocomposite films. Percentage of random nanodots versus nominal molar concentration N_p in the YBCO nanocomposites with MO = Y_2O_3, $BaZrO_3$, $BaCeO_3$ and Ba_2YTaO_6. Error bars were determined from the fit uncertainty in the corresponding data analysis.

the YBCO superconducting state is not modified, as demonstrated by high-field $H_{c2}(T)$ measurements.

YBCO–MO (MO = $BaZrO_3$, Y_2O_3, $BaCeO_3$ and Ba_2YTaO_6) nanocomposites grown by CSD are characterized by a high concentration of randomly oriented nanodots, and this fraction depends mainly on the oxide composition (MO). The epitaxial fraction shows mainly the {001} out-of-plane texture (that is, $(00l)_{MO} \parallel (00l)_{YBCO}$), whereas the in-plane texture varies depending on the MO phase. Fibre textures and other minor texture components were also observed. It has been therefore mandatory to quantitatively evaluate the randomly oriented fraction for all the investigated nanocomposites following a methodology[2] based on the simultaneous out-of-plane measurement of both the diffracted pole from the $(00l)$ epitaxial fraction and the diffraction ring from the randomly oriented fraction (Supplementary Information).

Figure 1 shows the percentage of randomly oriented nanodots in the YBCO–MO nanocomposites as a function of the nominal molar composition of MO N_p, as obtained with this methodology. Note that Y_2O_3 (YO) nanodots have a large fraction of epitaxial orientation, which decreases with the nanodot concentration, whereas $BaZrO_3$ (BZO), $BaCeO_3$ (BCO) and Ba_2YTaO_6 (BYTO) nanodots have a much higher randomly oriented fraction concentrating mainly within the YBCO matrix with only a small percentage remaining epitaxial at the substrate interface[2,14]. The observed differences are consistent with the increase of in-plane lattice mismatch of the four oxides with YBCO in a cube-on-cube epitaxy (−2.7%, +8.7%, +8.5% and +12.1% respectively), which enhances the possibility of avoiding epitaxial order[14].

The size of the randomly oriented nanodots in the different series of nanocomposite oxides was determined from transmission electron microscopy (TEM) images and it was found to be in the same range as the domain size of the epitaxial nanodots along the [001] direction, as estimated from the integral breadth of X-ray diffraction (XRD) reflections using the Scherrer formula[2] (Supplementary Information). Typical mean nanodot radii were estimated by TEM to be ∼15 nm, ∼15 nm, ∼25 nm and 7–20 nm for YO, BZO, BCO and BYTO, respectively. In the first three cases the crystallite size was found to be essentially independent of the nominal concentration in the nanocomposite whereas in the case of BYTO an increase of the nanodot size was detected with an increase of the secondary-phase concentration.

A key issue to engineer nanocomposite functionalities is to control strain. In epitaxial nanocomposites grown by *in situ* techniques[12] macroscopic strain is mostly shown; that is, the

mean value of lattice parameters is changed at the coherent or semi-coherent interfaces[19]. However, in *ex situ*-derived nanocomposites macroscopic strain is not shown, in agreement with the dominance of incoherent interfaces given by the large majority of randomly oriented secondary MO nanodots (Fig. 1). Instead, non-uniform strain (root mean squared, r.m.s., strain) is revealed and an accurate analysis of XRD peak broadening is required for its quantification.

As XRD peak broadening may arise from both the finite size of coherently diffracting domains (size effect) and non-uniform elastic distortions of the crystal lattice at the atomic level (strain effect), we need to use procedures that properly separate the two components. This is usually done by taking into account the different dependences on the reflection order.

Through the use of the so-called Williamson–Hall plot, the non-uniform strain can be determined[2]. However, this technique is only semiquantitative and it is usually difficult to extend to anisotropically strained samples because asymmetric diffraction lines are not available. In this work, although Williamson–Hall plots were used to investigate the trends with modified compositions[2], Rietveld refinement was carried out for some compositions in which both isotropic and anisotropic models of strain size are implemented (Supplementary Information; ref. 20).

Figure 2a shows typical Williamson–Hall plots from the $(00l)$ diffraction lines for nanocomposite films. Nanostrain values along the [001] crystallographic direction are easily determined from these plots, and as shown in Fig. 2b a single linear behaviour occurs with the incoherent specific interface of all nanodot series, whereas different dependences on nanodot concentration are followed for each series of nanocomposites (Supplementary Information). This latter parameter takes into account the percentage of random nanodots and the corresponding nanodot size. Hence, this demonstrates that the non-coherent interface between the nanodots and the YBCO matrix is the controlling parameter for the nanostrain generation. Figure 2b (magenta star) furthermore demonstrates that nanostrain already exists within YBCO after the growth process, before the oxygenation treatment. The enhanced efficiency of YBCO–BZO and YBCO–BYTO nanocomposites over those with YO in nanostrain generation is also reflected in the associated disorder of the YBCO matrix, estimated by the decrease of the out-of-plane texture quality (full-width at half-maximum of ω scan, $\Delta\omega$, increase with nanodot content) of the YBCO–BZO and YBCO–BYTO nanocomposites (Supplementary Information).

To evaluate the nanostrain not only for symmetric but also for asymmetric reflections, a Rietveld analysis of a set of symmetric and asymmetric reflections was carried out and the in-plane (ε_{xy}) and out-of-plane (ε_z) strain were determined for several nanocomposites. Results are presented following the expected elliptical behaviour (see Supplementary Information for further details). Figure 2c shows that, whereas the pristine YBCO films have an anisotropic r.m.s. strain with $\varepsilon_{xy}/\varepsilon_z \sim 2$, an isotropic nanostrain is achieved with BZO contents above 10 mol%. Simultaneously to the linear increase of the r.m.s. strain with the random fraction of nanodots, the Rietveld fits also showed that the coherent domain size of the YBCO lattice decreases linearly with this parameter (Fig. 2d). In the YBCO–BZO case, the domain size was found to be isotropic, and it was reduced from ∼200 nm to ∼100 nm when going from pure YBCO to 15 mol% BZO. This is a very significant reduction, which further confirms the nanometric scale of the generated r.m.s. strain of these nanocomposites.

Atomic-scale analysis with high-resolution scanning TEM (STEM) discloses the particular defects that have been found to enhance the r.m.s. nanostrain in the YBCO–MO nanocomposites. Figure 3 shows cross-sectional STEM images of a YBCO film where different types of BZO nanodot are identified. Figure 3a shows two BZO nanodot species embedded into the YBCO matrix:
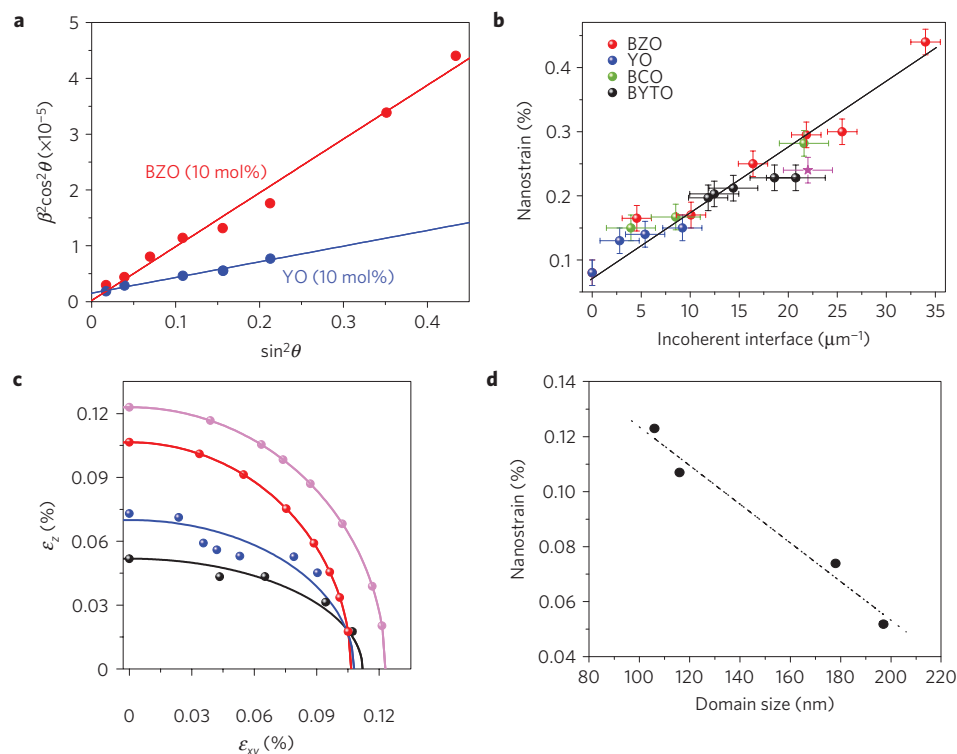
Figure 2 | Nanostrain analysis of the nanocomposite films by X-ray diffraction line-broadening analysis. a, Williamson–Hall plot of the symmetric YBCO Bragg reflections for YBCO–BZO (in red) and YBCO–YO (in blue) nanocomposites with 10 mol% nanodots. Nanostrain values along the normal film direction (vertical nanostrain) are determined from the linear fit of the symmetric YBCO (00l) Bragg peaks. Size effects are not significantly changing, as shown by the vanishing intercept in all cases. **b**, Dependence of the YBCO vertical nanostrain (determined from Williamson–Hall plots) on the incoherent specific interface of nanodots in the different nanocomposites (BZO, YO, BCO, BYTO), where both the percentage of random fraction and the nanodot size have been considered. Data from a 13 mol% BZO nanocomposite before oxygenation are also included (star symbol). **c**, Nanostrain anisotropy (determined from Rietveld analysis of high-resolution XRD data) for a pure YBCO film (black) and three nanocomposites with 10 mol% (red) and 15 mol% (pink) of BZO and 15 mol% (blue) of YO, respectively. **d**, Dependence of coherent domain size on nanostrain along the c axis in YBCO–BZO nanocomposites, as determined by Rietveld analysis of high-resolution XRD measurements. Error bars were determined from the fit uncertainty in the corresponding data analysis.

one nanodot corresponds to those nucleating onto the substrate surface and growing cube on cube with the YBCO (refs 21, 22), and the other corresponds to those randomly distributed within the YBCO matrix and essentially oriented at random, as indicated by XRD analysis (see Supplementary Information for further TEM images). The presence of the randomly distributed nanodots severely influences the microstructure of the YBCO–MO nanocomposites. Figure 3a–c shows that the YBCO matrix has a high density of intergrowths along the c axis (separated just a few nanometres) in the YBCO–BZO nanocomposite, well above that typically observed in YBCO thin films grown by CSD (refs 23, 24). These intergrowths consist mainly of an extra Cu–O chain layer, which can even form regions of ordered arrays of the $Y_2Ba_4Cu_8O_{16}$ (Y248) phase (Fig. 3c and inset). Nucleation of Y248 intergrowths occurs at incoherent interfaces and highly mismatched epitaxial interfaces (>15% nominal misfit[25]), such as those shown in Fig. 3c,d. These nanodots correspond to some of the minority orientation components observed in a detailed XRD texture analysis (A. Llordés *et al.* manuscript in preparation). It is worth noting that the BZO nanodots with highly mismatched interfaces (Fig. 3b) show faceted interfaces and they induce bending to the (00l)$_{YBCO}$ planes and nucleation of Y248 intergrowths. As epitaxial YBCO nucleation at the substrate interface is delayed, as compared with nucleation and growth of the randomly distributed BZO nanodots, the observed defect structure of the epitaxial YBCO matrix develops simultaneously with the nanodot reorientation and recrystallization of the YBCO–BZO interfaces. The driving force for this joint

microstructural rearrangement is the minimization of the high interfacial energy of incoherent interfaces. Occasionally, as shown in Fig. 3c,d (indicated by purple arrows), even two extra Cu–O chains are added, resulting in triple Cu–O chains corresponding to a local composition $YBa_2Cu_5O_8$ (ref 26). All these intergrowths cause a severe bending of (00l)$_{YBCO}$ planes and inhomogeneous strain in the YBCO lattice, which extend up to several unit cells. The triple Cu–O chain intergrowths are shorter in length (a few nanometres) when compared with the Y248 (tens to hundreds of nanometres), and so they have a stronger influence onto the local strain of the YBCO lattice. The dislocations surrounding the intergrowths enhance the nanostrain of the YBCO lattice, as we have estimated on specific regions through high-resolution Z-contrast images and using the Peak Pairs Analysis program, which computes the Ba–Ba and Ba–Y distances and calculates lattice strain maps (Supplementary Information; ref. 27). Figure 4 gives a specific example, where the three strain components, determined around two closely located intergrowths, are shown. The maps of strain components ε_{xx}, ε_{yy} and ε_{xy} are shown in Fig. 4c–e, respectively, for the area shown in Fig. 4a. Figure 4b shows, furthermore, the grid generated through the Peak Pairs Analysis algorithm in the same area. ε_{yy} shows the biggest change, specifically the intergrowth region, identified as a highly strained area ($\varepsilon_{yy} > 10\%$). Just above and below the intergrowths the Y–Ba perovskite block appears to be under a compressive strain compensating the increase in volume of the perovskite block with double chain (intergrowth). ε_{xx} shows striking changes of the a cell parameter alongside the
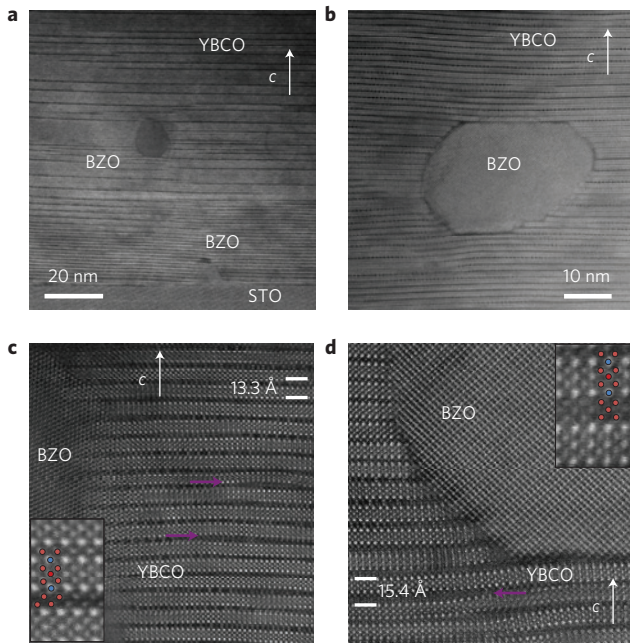
Figure 3 | Cross-sectional STEM micrograph of a YBCO nanocomposite thin film grown on STO along the [010] zone axis. a, Low-magnification Z-contrast images showing embedded BZO nanoparticles in the YBCO matrix. The horizontal dark stripes that cross the image are due to the Y248 intergrowths. **b**, Higher-magnification Z-contrast image showing the bending of the YBCO planes around the BZO nanoparticles. **c,d**, High-resolution Z-contrast images showing the interface between two different BZO nanoparticles with two different orientations and the YBCO matrix ($\langle 111 \rangle_{BZO} \parallel [100]_{YBCO}$ and $\langle 110 \rangle_{BZO} \parallel [010]_{YBCO}$ in **c** and $\langle 110 \rangle_{BZO} \parallel [001]_{YBCO}$ and $\langle 110 \rangle_{BZO} \parallel [100]_{YBCO}$ in **d**). These interfaces present a high density of Y248 intergrowths and cause a major distortion of the YBCO matrix. Purple arrows point to an intergrowth with two extra Cu-O chains added. The inset in **c** shows in detail the Y248 intergrowth, whereas the inset in **d** shows an intergrowth consisting of three Cu-O chains.

intergrowths. The lattice distortion extends up to ~2 nm from the intergrowths with a complex interaction pattern. The ripples present in the ε_{yy} map are due to the fact that in YBCO the Ba–Ba spacing is greater than the Ba–Y spacing. Overall, therefore, the analysis of the Z-contrast images confirms that the intergrowths lead to highly strained three-dimensional regions within the YBCO lattice. Further evidence of the disorder generated in the YBCO matrix is provided by conventional cross-section and plan-view images, enabling us also to estimate the typical lateral extension of Y248 intergrowths (Supplementary Information). The intergrowth diameters are found in the range ~50–100 nm, and considering that they are separated by ~2–3 nm along the c axis (Fig. 3) leads to a dislocation density ~ 1–5×10^{12} cm^{-2}, that is at least two orders of magnitude higher than the concentration observed in typical CSD YBCO films or melt-textured YBCO bulk ceramics[23,28].

Next, the relationship between nanoscale strain and vortex-pinning properties was investigated through extensive transport critical-current-density measurements. Figure 5a shows the magnetic-field dependences of the pinning force, $F_p = J_c(H) \times H$, measured at 77 K with $H \parallel c$, for several nanocomposite compositions as indicated, where a strong enhancement is observed for the nanocomposite films. Figure 5b reports the angular dependences of the critical current density $J_c(\theta)$ measured at 1 T and 77 K for different nanocomposites, where a strong reduction of the anisotropy is appreciated. To quantify the anisotropy the Blatter scaling approach has been applied to $J_c(\theta, H)$ and the irreversibility line $H_{irr}(\theta, T)$,

where an effective magnetic field is assumed, $H_{eff} = H\varepsilon(\gamma_{eff}, \theta)$, with $\varepsilon^2(\gamma_{eff}, \theta) = \cos^2(\theta) + \gamma_{eff}^{-2} \sin^2(\theta)$ and γ_{eff} an effective mass anisotropy. This scaling approach enables separation of the relative contributions of isotropic and anisotropic vortex-pinning contributions in superconducting materials, as indicated for the pinning force in a typical nanocomposite (Fig. 5c; refs 2,14,29; see also Supplementary Information).

Figure 5d shows a very relevant result: the weight of the isotropic contribution to the total vortex-pinning force at 77 K grows linearly with the nanoscale strain, independently of the nanodot composition, reaching in some cases a 100% weight. The modified efficiencies to enhance isotropic pinning of the different MO nanodot series arise mainly from the variation of the percentage of randomly oriented nanodots (mainly in YO) or from differences of nanodot sizes (BCO, BYTO and BZO). However, the evolution of the self-field critical current density J_c^{sf} with MO nanodot concentration is also found to require consideration (Fig. 5d inset). The incoherent interface of nanodots with the YBCO matrix, previously identified as the source of non-homogeneous strain generation (Fig. 2b), is found to be the key parameter for isotropic vortex-pinning control, not the nanodot concentration itself. However, at a certain stage the increase of nanodot concentration leads necessarily to a reduced percolating current density, and hence also a decrease of the pinning force. In addition, enhancing the concentration of randomly oriented nanodots degrades the YBCO lattice texture (Supplementary Information), thus also reducing J_c^{sf}. We may conclude that such a disorder plays some role in limiting J_c^{sf} by observing a smoother dependence of J_c^{sf} on YO concentration (Fig. 5d inset), a trend which correlates with a smaller influence of YO nanodots on the degradation of the YBCO texture quality. The most efficient series to enhance vortex pinning up to now is that based on BZO, which has a small nanodot size and keeps the highest J_c^{sf}. YBCO–BZO nanocomposites show the best combination between limited J_c^{sf} reduction and enhanced vortex pinning by nanostrain, thus leading to the highest value of pinning force observed so far, $F_p^{max} \sim 20$ GN m^{-3} (~10 mol% BZO). Beyond this concentration a decrease of the self-field critical current is observed in BZO and BYTO nanocomposites, even if the nanostrain can be further enhanced. These results suggest, therefore, that further increase of nanostrain contribution to F_p^{max} can in principle be induced by enhancing the incoherent specific interface; however, the blocking effect of the nanodots on the percolating current and/or the YBCO texture degradation needs to be minimized simultaneously.

Further support to the existing correlation between isotropic vortex-pinning strength and nanostrain has been obtained from the analysis of the relationship between γ_{eff} and the anisotropy of nanostrain. Figure 5e shows that the computed dependence of γ_{eff} on nanostrain follows a single plot for different concentrations and all the series (see also Supplementary Information). Whereas BZO nanodots induce a strong decrease of γ_{eff}, leading to a nearly isotropic vortex-pinning landscape, YO nanodots are much less effective for this purpose, and BCO and BYTO nanodots lie in the middle of the two trends. This behaviour supports our conclusion that the increase of the maximum isotropic pinning force for $H \parallel c$ is controlled by nanostrain (Fig. 5d). Furthermore, the inset of Fig. 5e shows that the decrease of γ_{eff} is related to the decrease of the r.m.s. nanostrain anisotropy determined by high-resolution XRD (Fig. 2c). The whole set of results, therefore, guides us to conclude that the enhanced strength of r.m.s. nanostrain and its decreased anisotropy are closely linked to the vortex-pinning strengthening and the decreased effective mass anisotropy γ_{eff} describing the isotropic term $J_c(\theta)$.

At this stage we could wonder if the results linking strain and vortex pinning derive from a modification of the intrinsic electronic properties of the YBCO crystal, or if the phenomenon results from
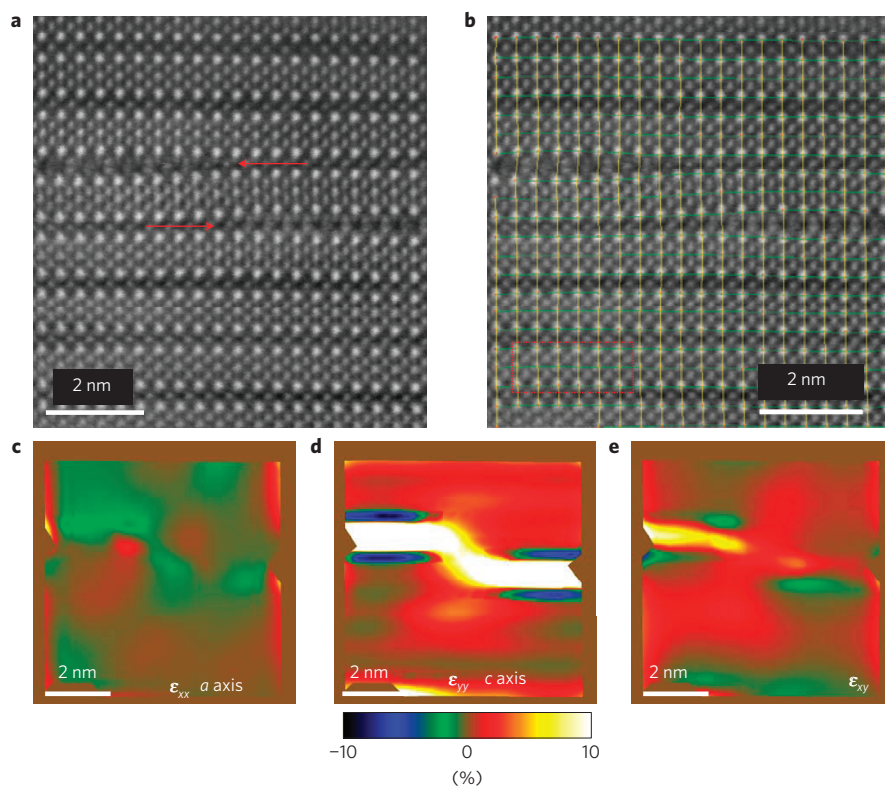
Figure 4 | Strain maps determined by Peak Pairs Analysis of cross-sectional STEM images showing intergrowths. a, Z-contrast image from which the strain maps were generated. The red arrows indicate two close intergrowths. **b**, Grid obtained by Peak Pairs Analysis from the image shown in **a**. The dotted red rectangle indicates the region of the image taken as reference. **c–e**, ε_{xx}, ε_{yy} and ε_{xy} maps, respectively.

a modified vortex-pinning landscape associated with a strained lattice. To clarify this fundamental issue we made isothermal magnetoresistance measurements under very high pulsed magnetic fields ($B_{max} = 40$ T; refs 30,31) to determine the upper critical field $\mu_0 H_{c2}(T)$ and hence to ascertain if the nanocomposites show any modification of the coherence lengths $\xi_0^i(H_{c2}(T) = \Phi_0/2\pi\xi^2(T))$ and $\xi(T) = \xi_0/(1 - T/T_c)^{1/2}$, where Φ_0 is the quantum flux and T_c the superconducting transition temperature) along $H \parallel c$ and $H \parallel ab$ and of the intrinsic superconducting anisotropy. Figure 6a shows a set of typical isothermal magnetoresistance, $R(H)$, measurements and the procedure followed to determine H_{c2}. The corresponding $H_{c2}(T)$ curves for $H \parallel c$ and $H \parallel ab$ are shown in Fig. 6b. A slight increase of ~10% in the corresponding $H_{c2}(T)$ curves is observed, and hence a corresponding decrease in the ξ_0^i values ($\xi_0^{ab} = 1.55$ nm and $\xi_0^c = 0.26$ nm in the 13% BZO nanocomposite), thus concluding that the intrinsic superconducting properties are not modified significantly. We also analysed the corresponding $H_{c2}(\theta)$ curves and we concluded that the intrinsic anisotropy of the nanocomposites is not modified, that is $\gamma \sim 5.9$–6.0 in both samples, whereas from vortex-pinning properties we obtain $\gamma_{eff} \sim 1.4$.

The different effective mass anisotropy γ_{eff} of the YBCO–MO nanocomposites within the vortex solid state ($H \leq H_{irr}(T)$), as compared with the intrinsic mass anisotropy γ determined in the vortex-liquid state (that is from $H_{c2}(T)$), where vortices can freely move, indicates that the quasi-isotropic superconducting vortex-pinning landscape generated by the nanostrain is not arising from a single quasispherical volume (γ_{eff} would remain equal to $\gamma \sim 5.9$–6.0) or from linear or planar defect geometries (contributing to $J_c^{aniso}(\theta)$ at specific orientations). Instead, a high density of ramified nanometric three-dimensional artificial pinning centres is required, enabling vortices to save line tension energy along a significant fraction of their length[23]. Here we propose that

the ramified strained three-dimensional network existing within the YBCO lattice is highly effective to generate a quasi-isotropic strong vortex-pinning landscape.

The upper-critical-field measurements enabled us to disregard any deep modification of the intrinsic superconducting properties of the YBCO crystal in the nanocomposites here studied, particularly its anisotropy. Thereof, we may wonder which microscopic physical mechanism can account for the strong coupling of lattice strain to pair formation, up to the level of creating nanoscale artificial pinning centres embedded within the YBCO lattice. First of all, we must exclude the possibility that the origin of the observed phenomenon may be associated with the conventional dependence of T_c on pressure. As was shown in ref. 32, YBCO has three different dependences of T_c on pressure along [100], [010] and [001] axes. In all cases $|dT_c/d\varepsilon_i| < 230$ K, where ε_i are the corresponding strain components, hence this mechanism would only locally decrease T_c by ~2 K. It was suggested, on the other hand, that in-plane tensile strain may impede the local oxygen ordering required to form the orthorhombic superconducting YBCO phase, and hence tetragonal insulating regions could be generated[15,33]. Our nanostrain maps obtained from high-resolution TEM images have shown that the fluctuations of c-axis lattice parameter have both signs and so they cannot be directly attributed to oxygen deficiency in the YBCO lattice, which would only increase the c axis parameter[34,35].

The existence of a direct strong influence of nanostrain on the superconducting order parameter is an unprecedented phenomenon in superconductivity. A new mechanism correlating the two phenomena[17], that is the bond-contraction pairing model, could eventually explain our experiments. This model stresses that a key role in the pairing mechanism should be attributed to the in-plane Cu–O distances, because hole pairing in adjacent Cu positions is made possible by the contraction of these bonds.
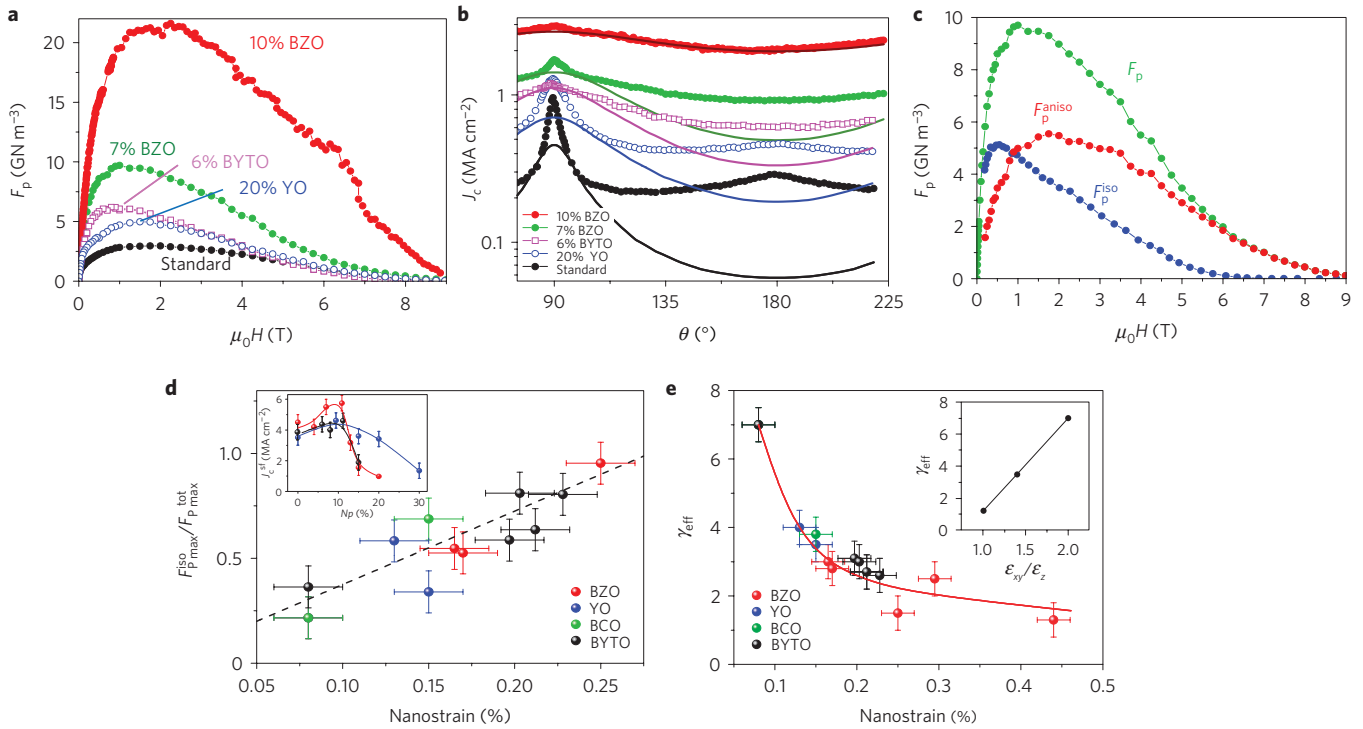
Figure 5 | Scaling of the pinning force and the mass anisotropy with the nanostrain. a, Pinning force versus magnetic field at 77 K in a series of nanocomposites. **b**, Angular dependence $J_c(\theta)$ measured at 77 K and 1 T for several nanocomposites. **c**, Separation of isotropic and anisotropic pinning-force components at 77 K in a typical nanocomposite. **d**, Dependence of the normalized maximum isotropic pinning force $F_{pmax}^{iso}/F_{pmax}^{tot}$ of all the nanocomposite series on the nanostrain determined from the Williamson–Hall plots. Inset: Dependence of the self-field critical current density at 77 K, J_c^{sf}, on the nominal nanodot concentration N_p in YBCO–MO (MO = BZO, YO, BYTO) nanocomposite series. **e**, Dependence of the effective mass anisotropy γ_{eff} determined from the isotropic pinning-defect contribution on the nanostrain deduced from the Williamson–Hall plot. Inset: Dependence of γ_{eff} on the ratio $\varepsilon_{xy}/\varepsilon_z$ determined from the anisotropic strain analysis in the YBCO–BZO nanocomposites. Error bars in γ_{eff}, H_{c2} and nanostrain were determined from the fit uncertainty in the corresponding data analysis. Error bars in J_c and F_p were determined from the uncertainty in the bridge width and film thickness.
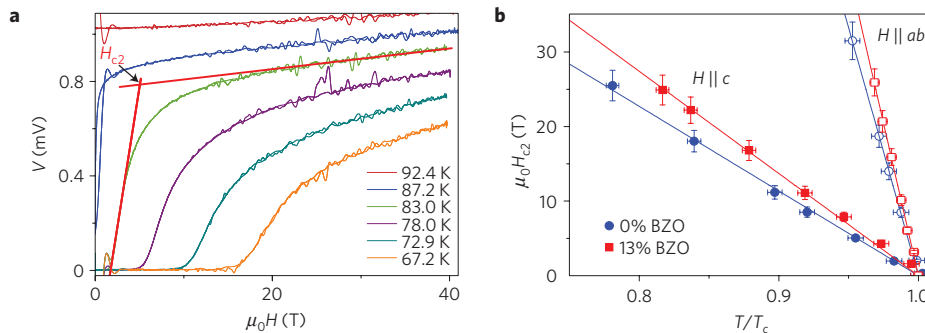

Figure 6 | High-field magnetoresistance measurements of H_{c2} anisotropy in a 13 mol% BZO nanocomposite. a, High-field isothermal $R(H)$ measurements made in pulsed magnetic fields up to $\mu_0H = 40$ T. The determination procedure of H_{c2} is indicated. **b**, $\mu_0H_{c2}(T)$ anisotropy in a YBCO and a 13 mol% BZO nanocomposite. Error bars were determined from the fit uncertainty in the corresponding data analysis and from the temperature uncertainty.

The pair-breaking energy 2Δ is the difference gained by pair formation and the energy of two carriers at the bottom of the conduction band

$$2\Delta = 4\frac{(t_{CuO})^2}{U} - 8t_0 \qquad (1)$$

where t_{CuO} is the transfer integral between a d orbital (Cu) and a p orbital (O) in the presence of doped holes, U is the on-site Coulomb repulsion and $4t_0$ is the half-bandwidth. The pairs are formed when the first term in the right-hand side of equation (1) overcomes the second one and so Δ is positive. Whereas Δ is known to be of the order of 50 meV in YBCO, both terms of equation (1) are in the range of 1 eV. Here t_{CuO} is very sensitive to the Cu–O

bond length ($t_{CuO} \propto 1/d_{CuO}^5$) and some elongation of Cu–O (~1% tensile strain) would quench the pair formation; that is, the second right term would overcome the first one in equation (1). This theory has successfully explained the weak-link behaviour observed for low-angle (<10°) grain boundaries in HTSs (ref. 36) taking into account the tensile strain associated with the dislocations[18,37], and justifies the detrimental effect of the grain-boundary tensile strain on J_c (ref. 15).

In conclusion, we report microstructural and critical-current investigation of a diverse series of nanocomposite superconducting thin films grown from chemical solutions, which has enabled the discovery of a new type of vortex-pinning mechanism in HTS materials. We have shown that inhomogeneous strain at

the nanoscale is responsible for a quasi-isotropic vortex-pinning force. We associate this previously unidentified pinning contribution with the generation of tensile strained regions where Cooper pair formation is precluded, thus becoming effective for pinning vortices. High-resolution STEM measurements indicate that dislocations surrounding intergrowths are the main factor responsible for a strained lattice. As a consequence, a nanoscale extended and disordered three-dimensional volume of strained YBCO lattice is formed, which draws a new contribution to the vortex-pinning landscape of HTSs.

Methods

Epitaxial c-axis-oriented YBCO and YBCO–MO (MO = BaZrO$_3$, Y$_2$O$_3$, BaCeO$_3$, Ba$_2$YTaO$_6$) nanocomposite thin films have been grown on single-crystalline LaAlO$_3$ and SrTiO$_3$ substrates. Samples were prepared from metallorganic precursor solutions with stoichiometric quantities of Y, Ba and Cu anhydrous trifluoroacetates, where Zr or Ce acetylacetonates, Ta ethoxide and/or Ba or Y anhydrous trifluoroacetates have been added to achieve the desired composition of the YBCO–MO nanocomposites. Here, MO molar contents have been modified in the range 0–20% mol. Further details on solution preparation, deposition and processing can be found in previous works[38–40].

Texture of the epitaxial films and quantitative determination of randomly oriented nanodot fraction were investigated with a Bruker-AXS D8 Advance diffractometer operating with Cu Kα radiation and equipped with a General Area Detector Diffraction System (see Supplementary Information for details). Non-uniform r.m.s. strain (nanostrain) was determined through XRD integral-breadth measurements, either through semiquantitative Williamson–Hall plots or from Rietveld analysis of a set of symmetric and asymmetric Bragg reflections to quantify the nanostrain anisotropy (see Supplementary Information for details). Error bars in the nanodot random fraction, incoherent interface and nanostrain are determined by the intensity and integral-breadth statistical uncertainty of Bragg reflections and the corresponding analytical fits. The nanoparticle size was determined by cross-sectional TEM studies. Two TEM systems were used in all the studies presented, a JEOL 2010F field-emission gun microscope and a FEI Tecnai F30 electron microscope operating at 300 kV. High-resolution high-angular annular dark-field STEM studies were carried out on a VG HB501UX microscope and a Nion UltraSTEM, both operated at 100 kV and equipped with a Nion aberration corrector. Specimens for STEM and conventional TEM were prepared by conventional methods, by grinding, dimpling and Ar ion milling. Atomic-resolution high-angular annular dark-field STEM studies on the planar-view prepared samples were obtained on a FEI Titan (60–300 kV) equipped with a probe-aberration corrector, a monochromator and an XFEG electron gun. Critical current densities were obtained either by inductive methods or by transport measurements. Inductive $J_c(H, T)$ values were obtained by applying to thin films the standard critical-state model. The hysteretic magnetization curves were measured with a commercial superconducting quantum interference device magnetometer and transport measurements were made in a 9 T cryostat. Narrow bridges in the range of 10 μm were fabricated by standard optical lithography with a typical width uncertainty of ±0.2 μm. Film-thickness uncertainty, determined by a three-dimensional profilometer, has been estimated to be ∼10%, leading to an overall estimated maximum error of ∼15% in the given J_c values. The metal contacts were evaporated and post-annealed, ensuring resistances below 10 μΩ, which enabled current–voltage, $I(V)$, transport measurements down to 5 K even for very high-J_c samples. The applied current was sent parallel to the ab planes and J_c was determined by using a 1 μV cm^{-1} criterion. The magnetic field was rotated from the c axis ($\theta = 0°$) to the ab plane ($\theta = 90°$) with an angle resolution better than 0.1°, always ensuring maximum-Lorentz-force configuration between the applied magnetic field and transport current. The angular-dependent irreversibility line was determined with a $\rho/\rho_N \approx 10^{-3}$ criterion with ρ and ρ_N being the resistivity and the resistivity at 100 K, respectively. It is worth mentioning that T_c was not altered in any of the YBCO–MO nanocomposites.

Angular-dependent resistivity measurements in high pulsed fields were made for the determination of H_{c2}. An a.c. current of 100 A cm^{-2} with a frequency of 39.9 kHz was applied in a 5 ms pulsed magnetic field up to 40 T. During the field pulses, the resistivity of the sample was measured at different temperatures for $H \parallel c$ and $H \parallel ab$. The value of H_{c2} at a given T was determined from the intersection field between the linear behaviour of $R(H)$ in the normal state and the linear (flux-flow) piece of $R(H)$ during the transition. Error bars in γ_{eff} and H_{c2} were determined from the fit uncertainty in the corresponding data analysis, as detailed in the text.

References

1. Campbell, A. M. & Evetts, J. E. Flux vortices and transport currents in type II superconductors. *Adv. Phys.* **21,** 199–428 (1972).
2. Gutiérrez, J. *et al.* Strong isotropic flux pinning in solution-derived YBa$_2$Cu$_3$O$_{7−x}$ nanocomposite superconductor films. *Nature Mater.* **6,** 367–373 (2007).
3. Macmanus-Driscoll, J. L. *et al.* Strongly enhanced current densities in superconducting coated conductors of YBa$_2$Cu$_3$O$_{7−x}$+ BaZrO$_3$. *Nature Mater.* **3,** 439–443 (2004).
4. Obradors, X. *et al.* in *Comprehensive Nanoscience and Technology* (eds Andrews, D., Scholes, G. & Wiederrecht, G.) (Elsevier, 2010).
5. Matsumoto, K. & Mele, P. Artificial pinning center technology to enhance vortex pinning in YBCO coated conductors. *Supercond. Sci. Technol.* **23,** 014001 (2010).
6. Foltyn, S. R. *et al.* Materials science challenges for high-temperature superconducting wire. *Nature Mater.* **6,** 631–642 (2007).
7. Kang, S. *et al.* High-performance high-T_c superconducting wires. *Science* **311,** 1911–1914 (2006).
8. Goyal, A. *et al.* Irradiation-free, columnar defects comprised of self-assembled nanodots and nanorods resulting in strongly enhanced flux-pinning in YBa$_2$Cu$_3$O$_{7−\delta}$ films. *Supercond. Sci. Technol.* **18,** 1533–1538 (2005).
9. Haugan, T., Barnes, P. N., Wheeler, R., Meisenkothen, F. & Sumption, M. Addition of nanoparticle dispersions to enhance flux pinning of the YBa$_2$Cu$_3$O$_x$ superconductor. *Nature* **430,** 867–870 (2004).
10. Blatter, G., Feigelman, M. V., Geshkenbein, V. B., Larkin, A. I. & Vinokur, V. M. Vortices in high-temperature superconductors. *Rev. Mod. Phys.* **66,** 1125–1388 (1994).
11. Teichert, C. Self-organization of nanostructures in semiconductor heteroepitaxy. *Phys. Rep. Rev. Sec. Phys. Lett.* **365,** 335–432 (2002).
12. MacManus-Driscoll, J. L. Self-assembled heteroepitaxial oxide nanocomposite thin film structures: Designing interface-induced functionality in electronic materials. *Adv. Funct. Mater.* **20,** 2035–2045 (2010).
13. Mele, P. *et al.* Ultra-high flux pinning properties of BaMO$_3$-doped YBa$_2$Cu$_3$O$_{7−x}$ thin films (M = Zr, Sn). *Supercond. Sci. Technol.* **21,** 032002 (2008).
14. Puig, T. *et al.* Vortex pinning in chemical solution nanostructured YBCO films. *Supercond. Sci. Technol.* **21,** 034008 (2008).
15. Van der Laan, D. C., Haugan, T. J. & Barnes, P. N. Effect of a compressive uniaxial strain on the critical current density of grain boundaries in superconducting YBa$_2$Cu$_3$O$_{7−\delta}$ films. *Phys. Rev. Lett.* **103,** 027005 (2009).
16. Van der Laan, D. C. *et al.* Effect of strain, magnetic field and field angle on the critical current density of YBa$_2$Cu$_3$O$_{7−\delta}$ coated conductors. *Supercond. Sci. Technol.* **23,** 072001 (2010).
17. Deutscher, G. & de Gennes, P. G. A spatial interpretation of emerging superconductivity in lightly doped cuprates. *C.R. Phys.* **8,** 937–941 (2007).
18. Deutscher, G. Origin of weak-link behavior of grain boundaries in superconducting cuprates and pnictides. *Appl. Phys. Lett.* **96,** 122502 (2010).
19. Birkholz, M. *Thin Film Analysis by X-ray Scattering* (Wiley–VCH, 2006).
20. Lutterotti, L. http://www.ing.unitn.it/~maud/
21. Abellán, P. *et al.* Interaction between solution derived BaZrO$_3$ nanodot interfacial templates and YBa$_2$Cu$_3$O$_7$ films leading to enhanced critical currents. *Acta Mater.* **59,** 2075–2082 (2011).
22. Gutierrez, J. *et al.* Anisotropic c axis pinning in interfacial self-assembled nanostructured trifluoroacetate–YBa$_2$Cu$_3$O$_{7−x}$ films. *Appl. Phys. Lett.* **94,** 172513 (2009).
23. Gutierrez, J. *et al.* The role of stacking faults in the critical current density of MOD films through a thickness dependence study. *Supercond. Sci. Technol.* **22,** 015022 (2009).
24. Holesinger, T. G. *et al.* Progress in nanoengineered microstructures for tunable high-current, high-temperature superconducting wires. *Adv. Mater.* **20,** 391–407 (2008).
25. Gibert, M. *et al.* Self-organized Ce$_{1−x}$Gd$_x$O$_{2−y}$ nanowire networks with very fast coarsening driven by attractive elastic interactions. *Small* **6,** 2716–2724 (2010).
26. Ramesh, R., Jin, S. & Marsh, P. Superconductor defect structure. *Nature* **346,** 420–420 (1990).
27. Galindo, P. L. *et al.* The Peak Pairs algorithm for strain mapping from HRTEM images. *Ultramicroscopy* **107,** 1186–1193 (2007).
28. Plain, J., Puig, T., Sandiumenge, F., Obradors, X. & Rabier, J. Microstructural influence on critical currents and irreversibility line in melt-textured YBa$_2$Cu$_3$O$_{7−x}$ reannealed at high oxygen pressure. *Phys. Rev. B* **65,** 104526 (2002).
29. Gutierrez, J., Puig, T. & Obradors, X. Anisotropy and strength of vortex pinning centers in YBa$_2$Cu$_3$O$_{7−x}$ coated conductors. *Appl. Phys. Lett.* **90,** 162514 (2007).
30. Ando, Y. *et al.* Resistive upper critical fields and irreversibility lines of optimally doped high-T_c cuprates. *Phys. Rev. B* **60,** 12475–12479 (1999).
31. Miura, M. *et al.* Vortex liquid–glass transition up to 60 T in nanoengineered coated conductors grown by metal organic deposition. *Appl. Phys. Lett.* **96,** 072506 (2010).
32. Welp, U. *et al.* Effect of uniaxial-stress on the superconducting transition in YBa$_2$Cu$_3$O$_7$. *Phys. Rev. Lett.* **69,** 2130–2133 (1992).

33. Chisholm, M. F. & Pennycook, S. J. Structural origin of reduced critical currents at $YBa_2Cu_3O_{7-\delta}$ grain-boundaries. *Nature* **351**, 47–49 (1991).

34. Ye, J. H. & Nakamura, K. Quantitative structure analyses of $YBa_2Cu_3O_{7-\delta}$ thin-films—determination of oxygen-content from X-ray-diffraction patterns. *Phys. Rev. B* **48**, 7554–7564 (1993).

35. Klie, R. F. *et al.* Enhanced current transport at grain boundaries in high-T_c superconductors. *Nature* **435**, 475–478 (2005).

36. Hilgenkamp, H. & Mannhart, J. Grain boundaries in high-T_c superconductors. *Rev. Mod. Phys.* **74**, 485–549 (2002).

37. Heinig, N. F., Redwing, R. D., Nordman, J. E. & Larbalestier, D. C. Strong to weak coupling transition in low misorientation angle thin film $YBa_2Cu_3O_{7-x}$ bicrystals. *Phys. Rev. B* **60**, 1409–1417 (1999).

38. Obradors, X. *et al.* Progress towards all-chemical superconducting $YBa_2Cu_3O_7$ coated conductors. *Supercond. Sci. Technol.* **19**, S1–S14 (2006).

39. Zalamova, K. *et al.* Smooth stress relief of trifluoroacetate metal–organic solutions for $YBa_2Cu_3O_7$ film growth. *Chem. Mater.* **18**, 5897–5906 (2006).

40. Puig, T. *et al.* Influence of growth conditions on the microstructure and critical currents of TFA-MOD $YBa_2Cu_3O_7$ films. *Supercond. Sci. Technol.* **18**, 1141–1150 (2005).

Author contributions

A.L., M.C., R.V., S.Y. and S.R. carried out the synthesis and basic structural characterization of the materials; A.L. and D.C. carried out the advanced analysis of texture and nanostrain of the films through X-ray diffraction; A. Palau, A. Pomar and V.R. made and analysed magnetic and transport measurements; A. Palau, J. Gutiérrez, J.V. and V.M. were in charge of the high-magnetic-field measurements and the corresponding data analysis; J. Gázquez, J.A., R.G., F.S., M.V. and C.M. made different contributions to the TEM observations and the corresponding image analysis and interpretation; G.D. was involved in the theoretical analysis and contributed to the interpretation of the experimental data; A.L. and J. Gázquez wrote parts of the Supplementary Information; T.P. and X.O. designed and supervised the experiments and the theoretical analysis, coordinated the data interpretation and wrote the manuscript. All the authors participated in the correction of the manuscript.

Additional information

The authors declare no competing financial interests. Supplementary information accompanies this paper on www.nature.com/naturematerials. Reprints and permissions information is available online at www.nature.com/reprints. Correspondence and requests for materials should be addressed to X.C.